JGR Solid Earth

Key Points:

- XKS and local S wave splitting analyses suggest splitting of sub-slab flow into two branches after passing the eastern edge of the slab
- One is a SE directed continuation of sub-slab flow after passing the slab edge, the other enters the mantle wedge and flows to the SW
- The two flow systems have nearly orthogonal directions, leading to weak azimuthal anisotropy in the vicinity of the slab edge

Correspondence to:
S. S. Gao,
sgao@mst.edu

Mantle Flow in the Vicinity of the Eastern Edge of the Pacific-Yakutat Slab: Constraints From Shear Wave Splitting Analyses

**Yuchen Yang[1], Stephen S. Gao[1] , Kelly H. Liu[1] , Fansheng Kong[1,2] , and Xiaofei Fu[3]**

[1]Geology and Geophysics Program, Missouri University of Science and Technology, Rolla, MO, USA, [2]Key Laboratory of Submarine Geosciences, State Oceanic Administration & Second Institute of Oceanography, Ministry of Natural Resources, Hangzhou, China, [3]College of Earth Science and Research Institute of Unconventional Oil and Gas, Northeast Petroleum University, Daqing, China

Abstract   To investigate the effects of a slab edge and varying slab geometry on the mantle flow systems beneath south central Alaska, a total of 971 pairs of teleseismic shear wave (SKS, SKKS, and PKS) and 65 pairs of local S wave splitting parameters (fast orientations and splitting times) are measured using data from the USArray and other networks. The Pacific-Yakutat slab edge separates two regions with different characteristics of the splitting measurements. The area to the west of the slab edge has greater splitting times and mostly trench parallel fast orientations, and the area to the east is dominated by smaller splitting times and spatially varying fast orientations. The spatial distribution of the splitting parameters and results of anisotropy layering and depth analyses can be explained by a model involving three flow systems. The sub-slab flow initially entraining with the shallow-dipping Yakutat slab deflects to a trench-parallel direction due to slab retreat and an increase in slab dip, and flows northeastward toward the slab edge, where it splits into two branches. The first branch enters the mantle wedge as a toroidal flow and flows southwestward along the slab, and the second branch continues approximately eastward. The flowlines of the toroidal and continued flow systems are approximately orthogonal to each other in the vicinity of the slab edge, producing the observed small splitting times and spatially varying fast orientations.

Plain Language Summary   Alaska is home to some of the largest earthquakes and violent volcanic eruptions on Earth. These natural hazards are mostly caused by the subduction of the Pacific Plate beneath the North American Plate along the Aleutian Trench. Such subduction has not only led to the rising of the magnificent mountain belts seen on the surface, but also caused the mantle beneath the lithosphere to flow. By analyzing elastic waves produced by earthquakes that are at least 9,000 km away from the study area and recorded by seismographs deployed in south central Alaska, we have established a flow model that can adequately explain the observations. The model suggests that materials beneath the subducting Pacific-Yakutat slab are driven northeastward by the southward retreat of the Aleutian Trench. At the eastern edge of the subducting slab, they split into two branches, with one continuing eastward and another going around the slab edge and entering the area above the slab. The observations and the new flow model can be used to better understand forces and processes inside the Earth, which are the ultimate reasons for the earthquakes and volcanoes in tectonically active areas such as south-central Alaska.

1. Introduction

The eastern terminus of the Pacific-Yakutat slab in south central Alaska (Figure 1) is characterized by the partial subduction of the Yakutat terrane (YT), which has its origin as an oceanic plateau with anomalous crust of more than 20 km thick (Christensen & Abers, 2010; Ferris et al., 2003; Worthington et al., 2012). The buoyancy of the subducted portion of the YT has led to flat and shallow subduction in the area from the trench to ~600 km inland (Eberhart-Phillips et al., 2006), where the slab resumes a steeper dip that is comparable to that of the neighboring normal oceanic slab (Figure 1). Slab rollback and southward trench migration of the "normal" Pacific slab west of the YT have been suggested by geodynamic modeling (Schellart et al., 2007), although the YT portion of the slab may not experience rollback due to its high buoyancy (Jadamec & Billen, 2012). Recent seismic tomography and receiver function studies suggest that the
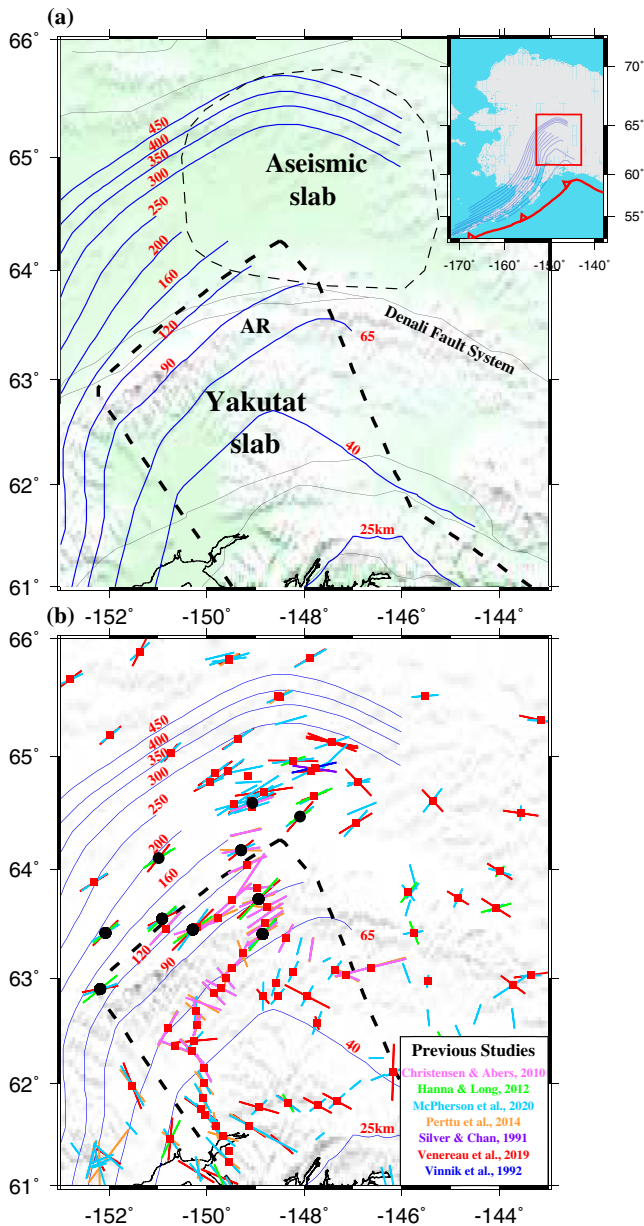
Figure 1. (a) Topographic relief map of the Alaska-Yakutat slab edge region with major geological structures. The Yakutat slab is delineated by the thick black dash line (Eberhart-Phillips et al., 2006), while the thin dash line indicates the aseismic slab area imaged by Gou et al. (2019). Contour lines of the depth of the Pacific slab are shown in blue (Gou et al., 2019). AR: Alaska Range. The upper right inset shows the location of the study area, which is outlined by a red rectangle. The red sawteeth mark the trench of the Alaska-Yakutat subduction zone. (b) Measurements from previous shear wave splitting studies labeled in the lower-right inset (Christensen & Abers, 2010; Hanna & Long, 2012; McPherson et al., 2020; Perttu et al., 2014; Silver & Chan, 1991; Venereau et al., 2019; Vinnik et al., 1992). Red squares and black dots mark the stations with XKS and local S measurements in this study, respectively.

Pacific-Yakutat slab may plunge into a depth of over ∼400 km in the mantle (Dahm et al., 2017; Gou et al., 2019; Jiang et al., 2018; Martin-Short et al., 2018). Seismic tomography studies reveal a sharp slab edge that is consistent with the eastward termination of the Wadati-Benioff zone (e.g., Martin-Short et al., 2018), while some other studies argue that the slab edge may extend further to the north in the area underlain by an aseismic section of the slab (Figure 1; e.g., Gou et al., 2019).

Numerous geodynamic modeling investigations demonstrate that slab rollback near a slab edge can induce a toroidal component of mantle flow, which enters the mantle wedge from the sub-slab region (Jadamec & Billen, 2010, 2012; Kincaid & Griffiths, 2003; Stegman et al., 2006). Specifically for the study area in south central Alaska, Jadamec and Billen (2012) conduct mantle flow modeling by considering a set of slab geometry and rheology parameters. For virtually all models, a flow system associated with the Pacific-Yakutat slab edge is revealed. In particular, based on azimuthal anisotropy measurements from the Moho to 200 km depth, a recent Rayleigh wave tomography study (Feng et al., 2020) suggests a flow system that continues toward the southeast after coming out from the slab edge.

One of the most effective techniques to provide direct constraints on mantle flow models is shear wave splitting (SWS) analysis (Hess, 1964; Silver & Chan, 1991). It has long been recognized that when a P-to-S converted wave from the core-mantle boundary (SKS, SKKS, and PKS, hereafter collectively called XKS) propagates through an azimuthally anisotropic layer, the shear wave would split into two components with orthogonally polarized directions and different traveling speeds (Ando, 1984; Silver & Chan, 1991). Two splitting parameters, the polarization orientation of the fast component (ϕ or fast orientation) and the arrival time difference between the fast and slow components (δt or splitting time), are measured to quantify the orientation and strength of the seismic azimuthal anisotropy, respectively.

The primary mechanism for the generation of seismic anisotropy in the upper mantle is the lattice preferred orientation (LPO) of the crystallographic axes of anisotropic minerals, especially olivine (Zhang & Karato, 1995). Under normal temperature and pressure conditions, progressive simple shear will result in the fast polarization orientation to be parallel to the a-axis of olivine (Ribe & Yu, 1991). Simple shear is commonly produced by the relative movements between the lithosphere and asthenosphere such as those associated with absolute plate motion and slab subduction (Long & Becker, 2010; Schellart, 2004; Silver & Chan, 1991). Additionally, the a-axis aligns at a right angle to the direction of maximum horizontal compression under uniaxial compression (Ribe & Yu, 1991).

In a subduction zone configuration, XKS splitting measurements mainly reflect the combined contributions from the mantle flows in the sub-slab region and the mantle wedge (Long & Silver, 2009; Perttu et al., 2014), although contributions from the slab and the lithosphere of the overriding plate cannot be completely excluded (Feng et al., 2020; Kong et al., 2020; Tian & Zhao, 2012). Trench-parallel flow in the sub-slab region is commonly attributed to slab rollback, which may also be responsible for trench-perpendicular corner flow in the mantle wedge (e.g., Fouch & Fischer, 1996; Kong et al., 2020; Long & Silver, 2008, 2009; Russo & Silver, 1994). Away from the trench, trench-perpendicular entrained flow caused by viscous coupling between

the slab and the underlying mantle has been proposed (Currie et al., 2004; Eakin & Long, 2013; Paczkowski et al., 2014; Russo & Silver, 1994). Numerous shear wave splitting measurements in the vicinity of a slab edge can be explained by edge induced toroidal flow (Civello & Margheriti, 2004; Hanna & Long, 2012; McPherson et al., 2020; Palano et al., 2017; Venereau et al., 2019).

Most XKS splitting studies including those conducted in Alaska (e.g., Christensen & Abers, 2010; Hanna & Long, 2012; Perttu et al., 2014; Venereau et al., 2019) were conducted under the assumption of simple anisotropy, which refers to anisotropy from a single anisotropic layer with a horizontal axis of symmetry (Silver & Chan, 1991). This ideal condition produces similar splitting parameters with respect to the arriving azimuth of the events (back-azimuth or BAZ). Departures from the ideal conditions of simple anisotropy are termed as complex anisotropy (Silver & Savage, 1994), and the most common form of complex anisotropy structure consists of two anisotropic layers, each with a horizontal axis of symmetry. The two-layered complex anisotropy is characterized by systematic azimuthal variations of the individual splitting parameters with a 90° periodicity. Additionally, if a station is located near the boundary between two or more areas with different anisotropic characteristics, the observed anisotropy at the station may also vary azimuthally (referred to as spatially varying anisotropy hereinafter), although the variation may not necessarily possess a 90° periodicity (Alsina & Snieder, 1995; Liu & Gao, 2013).

2. Previous SWS Studies and Rationale of the Present Study

A number of previous SWS studies have been carried out in the Alaska region (Figure 1b), elucidating some significant mantle flow features in the vicinity of the Pacific-Yakutat slab edge. The most prominent feature observed by pre-USArray studies (Christensen & Abers, 2010; Hanna & Long, 2012; Perttu et al., 2014) in this region is an ~90° change in the observed fast orientation near the ~70 km slab depth contour line, which separates the northern area with mostly trench-parallel fast orientations and the southern area that is dominated by trench-perpendicular orientations. The two clusters of fast orientations are mostly interpreted as reflecting along-strike flow in the mantle wedge and trench-perpendicular flow in the sub-slab region, respectively. Using data from some of the USArray and other stations, Venereau et al. (2019) and McPherson et al. (2020) conduct SWS investigations in the entire Alaska region. Both studies observe a circular pattern in the vicinity of the slab edge, and attribute the observations to an edge-induced toroidal flow system. Furthermore, on the basis of the consistency between the fast orientations and the strike of strike-slip faults (e.g., Denali Fault, Figure 1a), the observed anisotropy near the fault zones is considered to be related to shear strain generated by the relative motion along the faults (McPherson et al., 2020).

The current study was motivated by a number of factors. First, most of the previous SWS studies focus on identifying the different mantle flow systems in southern Alaska or the entire Alaska region (Hanna & Long, 2012; McPherson et al., 2020; Venereau et al., 2019), and detailed analyses focused on the mantle flow systems associated with the slab edge are lacking. Second, complex anisotropy (mostly in the form of multi-layered anisotropy) has not been recognized in the study area due to a lack of adequate azimuthal coverage. Third, local S wave splitting analysis, which is an effective tool in discriminating wedge and sub-wedge anisotropy (e.g., Karlowska et al., 2021; Kong et al., 2020), is scarce in this region. Fourth, due to the near-vertical incidence of the XKS phases, the depth of the source of the observed XKS splitting remains ambiguous. Fifth, some aspects of the mantle flow systems in the slab edge region, including the lateral extent of the toroidal flow and the existence or absence of an eastward continuation of the sub-slab flow after it comes out of the slab edge, are still not well understood (Feng et al., 2020; Hanna & Long, 2012; Jadamec & Billen, 2010; Venereau et al., 2019).

In this study, we take advantage of the recent significant improvement in both the station and azimuthal coverages in the study area as a result of the USArray deployment to systematically investigate the mantle flow system in south central Alaska. We isolate contributions of sub-slab anisotropy to the observed SWS using local S wave splitting analysis, estimate the depth of the source of XKS splitting using a spatial coherency approach (Gao & Liu, 2012; Liu & Gao, 2011), grid-search the two pairs of splitting parameters under a two-layered model (Silver & Savage, 1994), and propose a new mantle flow model to explain the observed seismic anisotropy.
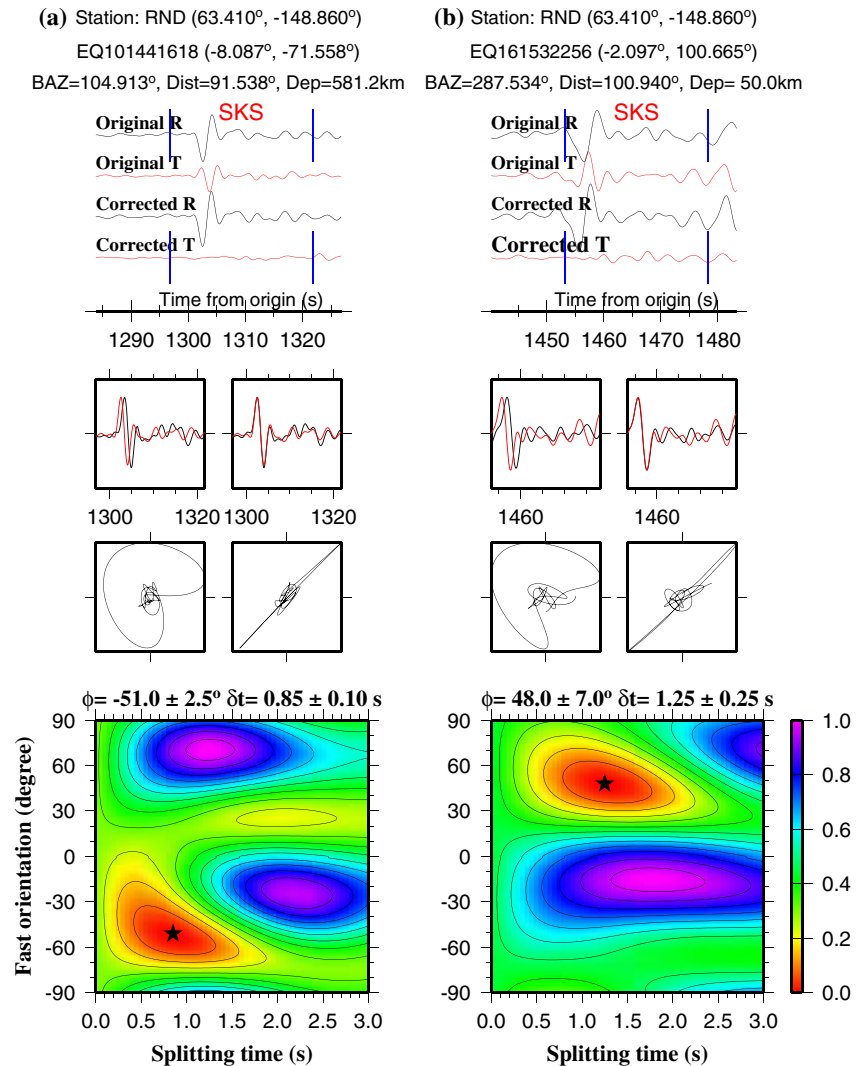
Figure 2. Examples of shear wave splitting measurements from two events recorded by station RND. The plots in the top row show original and corrected radial and transverse components, and plots in the central rows show the fast and slow waveforms and particle motions. The bottom plots are misfit maps, in which colors represent the normalized energy on the corrected transverse component. The optimal pair of splitting parameters corresponds to the minimum value on the misfit map and is marked by the black star. Note the significant differences in the splitting parameters from the two events recorded by the same station due to different piercing point locations.

3. Data and Methods

The XKS and local S data used in this study were recorded by 106 broadband seismic stations (Figure 1b) located in the area of 61–66°N and 153–143°W, covering a recording period of 30 years from late 1988 to October 2019. The epicentral distance range is 83°–180°, 95°–180°, and 120°–180° for SKS, SKKS, and PKS, respectively (Liu & Gao, 2013). In comparison, the latest SWS study covering the study area (McPherson et al., 2020) used only the SKS phase in the distance range of 80°–140° recorded during the period of early 2010 to middle 2017. The seismic data used in this study were recorded by a total of 11 networks specified in the Data Availability Statement and were archived at and requested from the Incorporated Research Institutions for Seismology (IRIS) Data Management Center (DMC).

The splitting parameters were measured and ranked following the procedures described in Liu and Gao (2013) for XKS and Jiang et al. (2021) for local S waves, and are briefly summarized below. For XKS splitting, the procedures were developed based on the minimization of transverse energy technique (Silver & Chan, 1991). Events with a magnitude of 5.6 or greater determined by the United States Geological
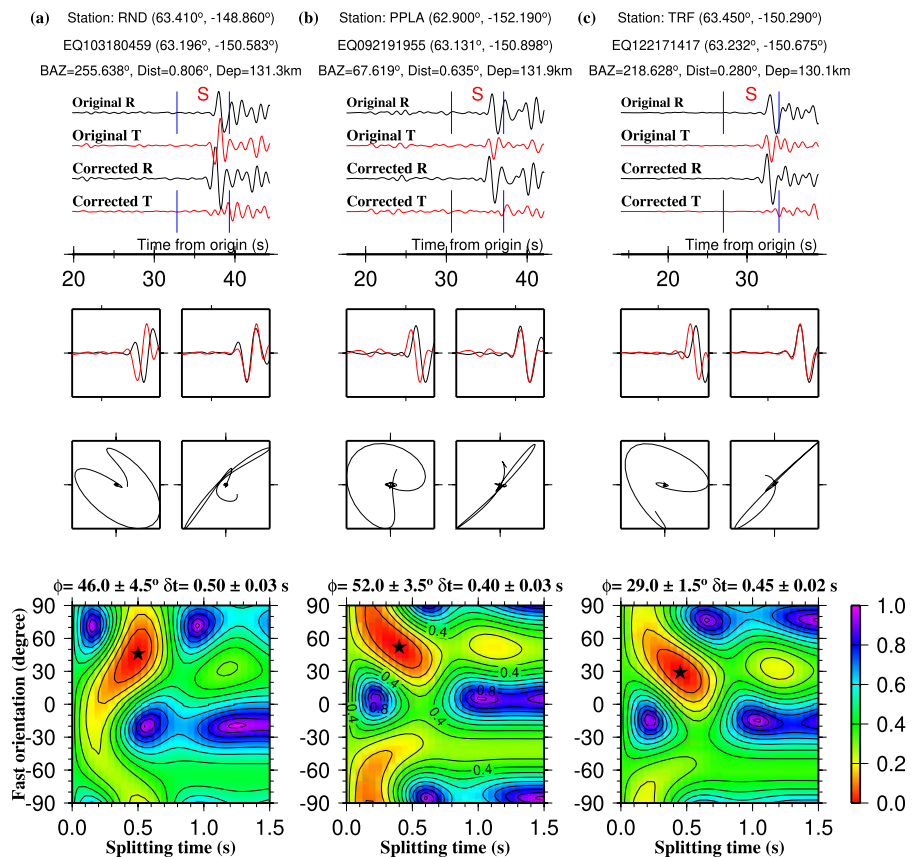
Figure 3. Same as Figure 2 but for local S measurements from stations (a) RND, (b) PPLA, and (c) TRF. Note that the original and corrected radial and transverse components are relative to the pre-splitting shear wave polarization orientation rather than the back azimuth of the event.

Survey (USGS) were used for data requesting from the DMC, and the cutoff magnitude was reduced to 5.5 for events with focal depths larger than 100 km. For local S wave splitting analysis, only local events with a magnitude of 4.0 and greater in the USGS catalog occurred in the S-wave window (which is approximately within an angle of incidence of 35°) were used, and the splitting parameters were measured using the principle of minimizing the lesser of the two eigenvalues of the covariance matrix (Silver & Chan, 1991). The focal depth of the local events resulting in one or more splitting measurements ranges from ∼80 to 145 km.

For XKS splitting, the seismograms were initially windowed in the time period 5 s before and 20 s after the predicted time of the XKS arrival, and were band-pass filtered in the frequency range of 0.04–0.5 Hz. The corresponding parameters for local S splitting are 5 s before and 10 s after, and 0.1–1.0 Hz. After all the splitting parameters were automatically calculated and ranked, we manually checked all the measurements to verify and (if necessary) adjust the beginning and end times of the XKS and local S window, quality ranking, and band-pass filtering frequencies. The final SWS measurements were grouped into Quality A (outstanding), B (good), N (null), and C (not used) using a set of criteria established based on the signal to noise ratios of the original radial, original transverse, and corrected transverse components (Liu et al., 2008), and only A and B measurements were used in the study. Null measurements, which are characterized by robust XKS arrival on the original radial but no XKS energy on the original transverse components, were not used in the study because all the stations with clear XKS arrivals on the radial components resulted in at least one Quality A or B measurement. Figure 2 exhibits example XKS measurements recorded at station RND from two events with different back azimuths, while Figure 3 shows local S wave splitting measurements from three different stations.
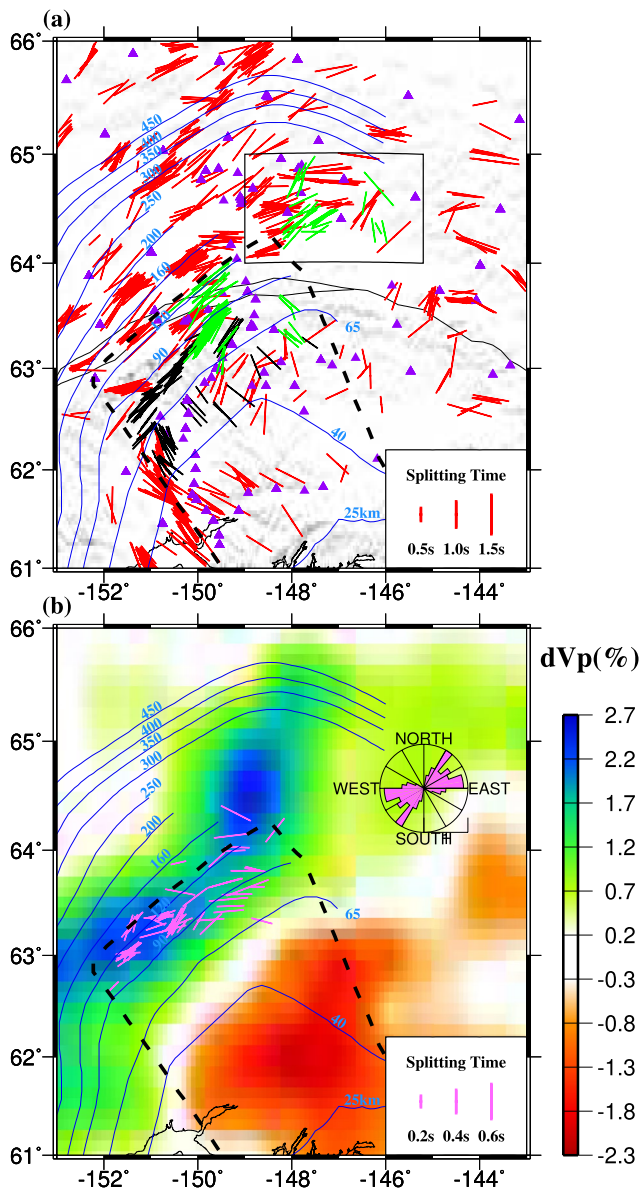
Figure 4. (a) 971 pairs of XKS splitting measurements from this study. Red bars stand for the splitting measurements from stations with azimuthally invariant measurements, black bars represent the splitting results showing systematic azimuthal variations with a 90° periodicity, and green bars indicate the splitting results exhibiting azimuthal variations without a 90° periodicity. All the measurements are plotted at the surface projections of the ray-piercing points at the depth of 200 km. Measurements from stations (purple triangles) in the black rectangle are used for anisotropy depth analysis shown in Figure 7. (b) 65 pairs of local shear wave splitting measurements and the rose diagram of the fast orientations. The background color shows the P wave velocity anomaly at 200 km depth (Gou et al., 2019).

4. Results

In total, 971 pairs of well-defined (Quality A or B) XKS measurements (Figure 4a) were obtained at 106 stations, while 65 pairs of local S measurements (Figure 4b) were measured at 10 stations. For the XKS results, the fast orientations have a circular mean value of 55.0° ± 37.4° and the splitting times range from 0.40 to 2.15 s with an average of 1.14 ± 0.31 s, which is slightly larger than the global average of 1.0 s for continents (Silver, 1996). For the local S splitting measurements, the averages are 62.4° ± 27.1° and 0.39 ± 0.13 s for the fast orientations and splitting times, respectively.

4.1. Characterization of Complex Anisotropy

Two-layered anisotropy is characterized by a 90° periodic variation of the individual splitting parameters and the two pairs of splitting parameters can be determined using a grid-searching technique (Silver & Savage, 1994). Similar to previous complex anisotropy studies (e.g., Cherie et al., 2016; Kong et al., 2018; Yang et al., 2014), measurements from 10 nearby stations with similar azimuthal variations (Figure 5) are combined in this study to improve the azimuthal coverage of the XKS events (black bars in Figure 4a). The resulting upper layer fast orientation is 47° which is nearly trench-parallel and has a splitting time of 0.7 s, while the fast orientation for the lower layer is 8° with a splitting time of 0.6 s (Figure 5).

Measurements from several stations (green bars in the black rectangle in Figure 4a) also exhibit azimuthal variations but without a 90° or 180° periodicity (Figure 6), indicative of possible existence of spatially varying (or piercing-point dependent) anisotropy. All the measurements from the northwest are trench-parallel, similar to the local S results, while those from the southeast are nearly NW-SE. Spatially varying anisotropy may reflect one anisotropy layer with different anisotropic characteristics (Alsina & Snieder, 1995; Jia et al., 2021; Liu & Gao, 2013), thereby implying a possible boundary that separates two or more areas with different anisotropy properties. We apply the spatial coherency approach to estimate the depth of the source of the observed anisotropy (Gao & Liu, 2012) using measurements from stations in the black rectangle in Figure 4a. To search for the optimal depth, the area is divided into overlapping blocks of dx by dx degrees² in size. The dx value ranges from 0.22° to 0.30° with a 0.02° interval. For each candidate depth, the coordinates of the ray piercing points for all the measurements are computed based on the 1-D IASP91 Earth model (Kennett & Engdahl, 1991). The standard deviations of the splitting parameters over all the measurements with ray piercing points inside each of the blocks are computed and then averaged over all the blocks. The optimal anisotropy depth corresponds to the highest spatial coherency which is reflected by the lowest spatial variation factor, which is defined as $F_v = w_\phi F_\phi + w_{\delta t} F_{\delta t}$, where F_ϕ is the mean standard deviation of the fast orientations, $F_{\delta t}$ is the mean standard deviation of the splitting times, w_ϕ and $w_{\delta t}$ are the weighting factor for the ϕ and δt measurements, respectively.

In this study, the optimal anisotropy depth is searched in the range of 0–350 km with an interval of 5 km. The weighting factor for ϕ is set as 1/180 and that for δt is set as 1/2.0 (because ϕ varies from 0 to 180° and δt has an approximate maximum value of 2.0 s). The anisotropy depth results are shown in Figure 7, in which
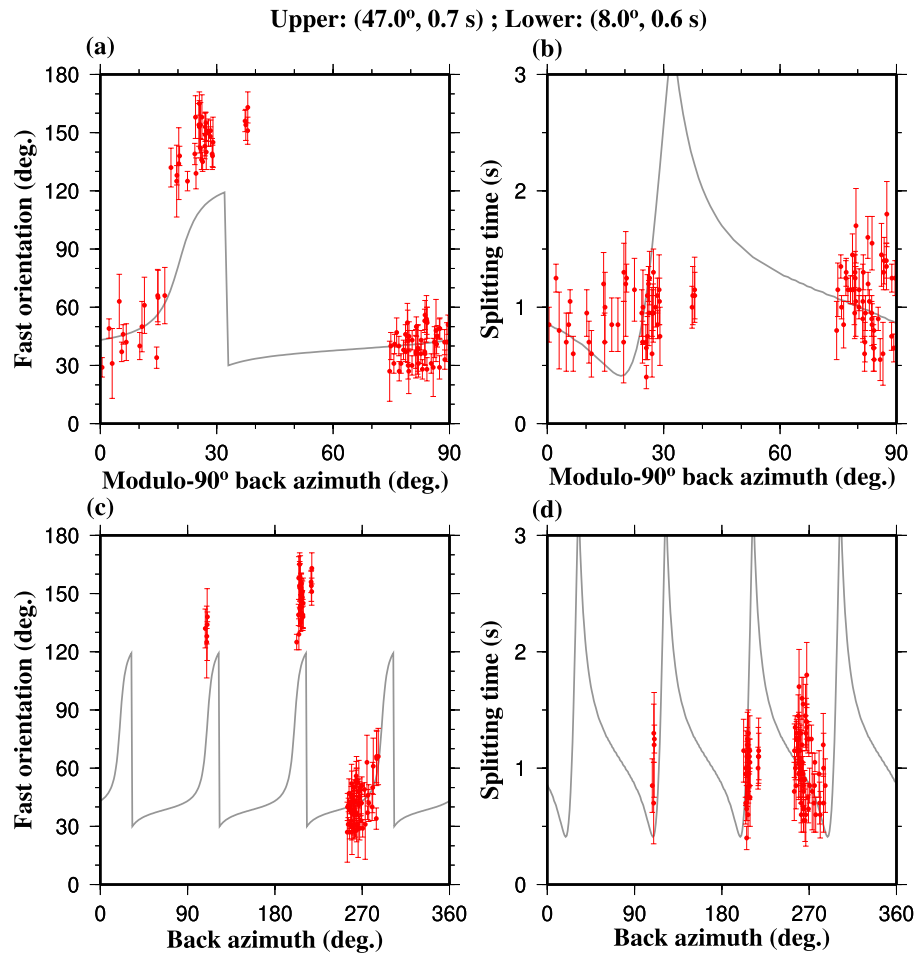
Figure 5. Systematic azimuthal variation of the combined XKS splitting measurements (black bars in Figure 4a). (a) Fast orientations plotted against modulo-90° back azimuth. (b) Splitting times against modulo-90° back azimuth. (c) Fast orientations against back-azimuth. (d) Splitting times against back-azimuth. The gray line in each plot represents the theoretical apparent splitting parameters calculated using the resultant optimal two pairs of parameters shown at the top of the figure.
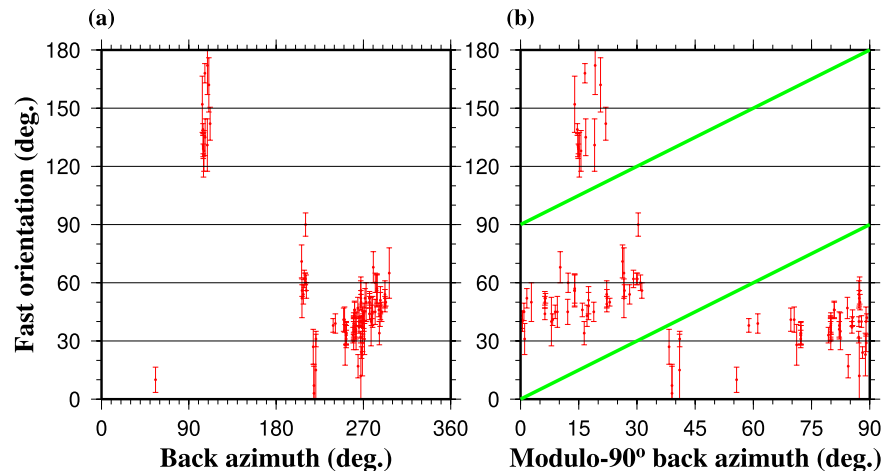
Figure 6. Azimuthal variation of the combined measurements (green bars in Figure 4a) showing spatially varying anisotropy. (a) Fast orientations against the back azimuth. (b) Fast orientations against modulo-90° back azimuth.
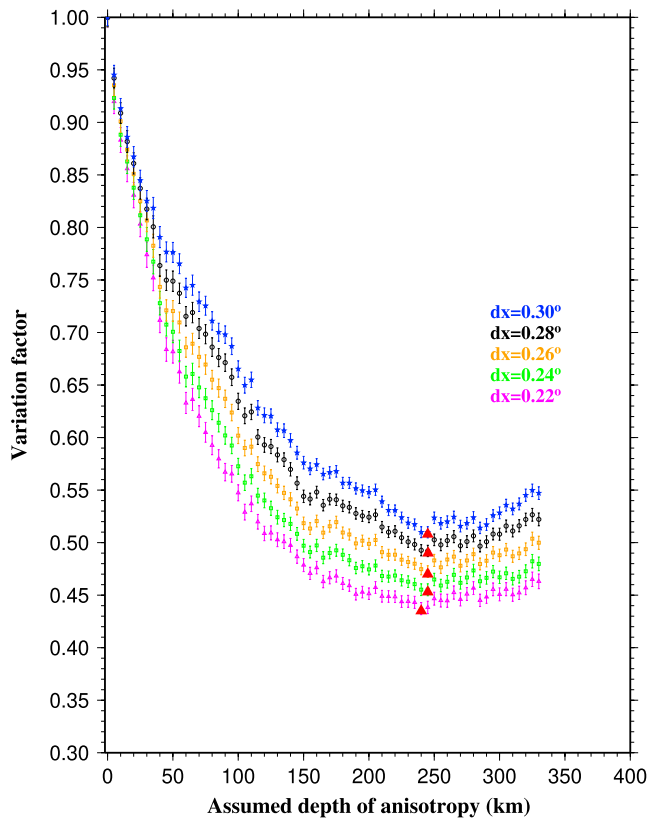
Figure 7. Spatial variation factors plotted against assumed depth of anisotropy for the XKS splitting measurements from stations in the region outlined by the black rectangle in Figure 4a. Different curves are obtained using different dx values. The red triangles on the curves represent the minimum variation factors corresponding to the optimal depths of anisotropy.

all spatial variation factor curves computed using different dx values indicate an estimated depth of ∼250 km, comparable with the regional slab depth proposed by seismic tomography studies (e.g., Gou et al., 2019). Note that because the 1-D IASP91 Earth model is used for ray tracing, the actual ray piercing locations at a given depth might be slightly different from the locations determined using the 1-D model when a realistic 3-D shear velocity model is used for ray tracing. Specifically relevant to the resulting F_ν is the situation that a piercing point determined (using the 1-D model) to be near the edge of a dx by dx degree^2 block may actually locate in a neighboring block. However, given the spatially gradual (relative to the size of the blocks) variation of the splitting parameters and the fact that only a small fraction of the piercing points are expected to be located near the edges, using a 3-D model should not significantly alter the resulting optimal depth. Such a gradual variation is the result of the large Fresnel zone relative to the block size (Alsina & Snieder, 1995; Chevrot, 2006; Jia et al., 2021).

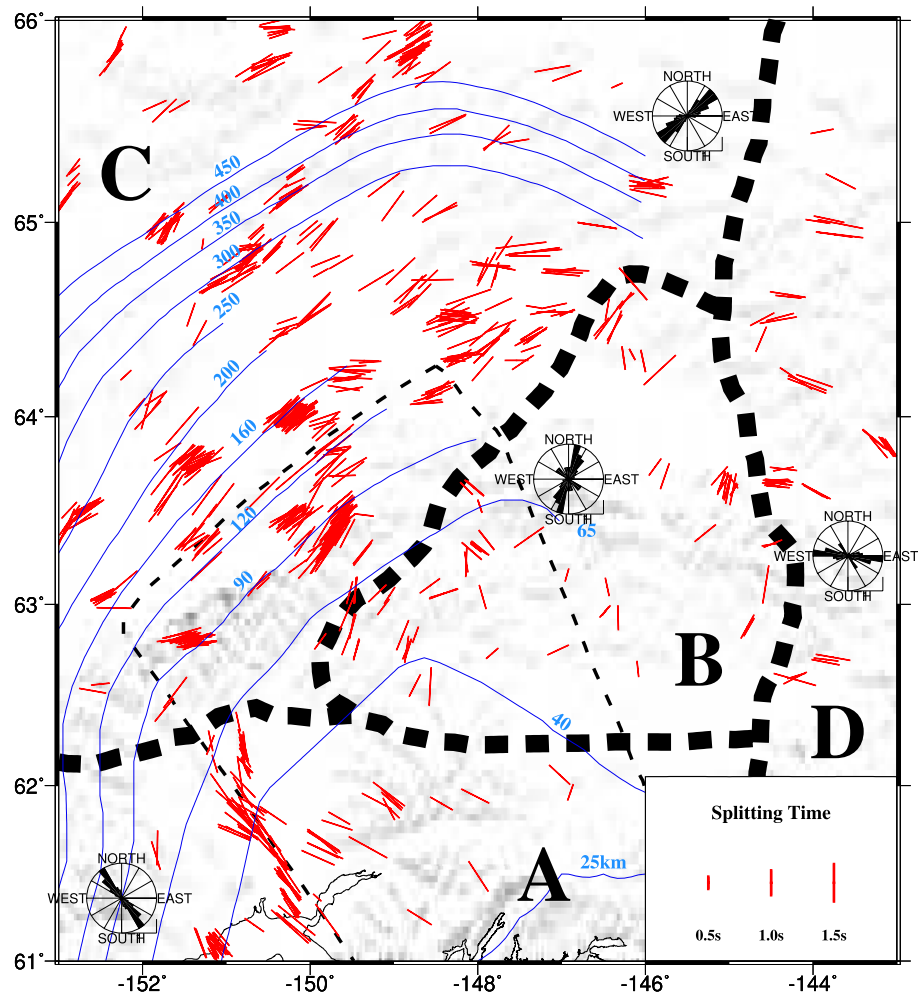### 4.2. Spatial Distribution of the Splitting Observations

The study area is divided into 4 sub-regions (Figure 8) based on the characteristics of the XKS measurements. Area A includes the southernmost portion of the subducted YT and includes 138 measurements from 18 stations. The circular mean of the fast orientations is 140.7° ± 14.8° and the mean splitting time is 1.15 ± 0.31s, both are consistent with those obtained by previous studies (Christensen & Abers, 2010; Hanna & Long, 2012; McPherson et al., 2020; Venereau et al., 2019). Almost all the stations located south of the ∼40 km slab depth contour line show trench-perpendicular fast orientations, which change to a nearly N-S direction where the slab descends more steeply.

Area B includes the NE portion of the YT and an area east of the Pacific-Yakutat slab edge, with 67 measurements from 14 stations. The mean values of the fast orientations and the splitting times are 15.3° ± 37.5° and 0.90 ± 0.27 s, respectively. The standard deviation of the fast orientations is the largest, and the mean value of the splitting times is the lowest, among the four regions. The YT portion of this area is dominated by NE-SW fast orientations, while fast orientations in the eastern part of the area, which is located to the immediate east of the slab edge, are mostly N-S.

Area C includes most part of the steeply dipping portion of the Pacific-Yakutat slab. The area contains 640 measurements from 47 stations. The circular mean of the fast orientations is 55.4° ± 20.5° and the simple mean of the splitting times is 1.17 ± 0.11 s, which is the highest in the study area. The fast orientations show a general parallelism with the strike of the slab depth contours, that is, NE-SW in the western part of the area and gradually rotate to E-W and then WNW-ESE near the slab edge, similar to those obtained from previous SWS studies (McPherson et al., 2020; Venereau et al., 2019). This region contains all the 65 pairs of local S splitting measurements from 10 stations (Figure 4b), with mean values of 62.4° ± 27.1° and 0.39 ± 0.13 s for the fast orientations and splitting times, respectively. At the same 10 stations, the average XKS fast orientation is 53.2° ± 27.1°, which is similar to the average fast orientation of local S results, and the mean splitting time is 1.25 ± 0.30 s, which is much larger than that of the local S results.

Area D is the easternmost part of the study area and includes 43 measurements from five stations. It is differentiated from Areas B and C by its dominantly WNW-ESE fast orientations (with a mean value of 100.1° ± 23.1°), similar to those in the northeastern part of Area C. The mean splitting time is 1.10 ± 0.32 s.

Figure 8. Subdivision of the study area based on the spatial distribution of XKS splitting measurements. All the measurements are plotted above the 200 km ray-piercing points. Black dash lines are the boundaries between the subregions (A–D). Each rose diagram indicates the fast orientations in each subregion.

5. Discussion

The major features of the XKS and local S splitting measurements as well as results from two-layer fitting and depth estimate can be accounted for by a model involving three flow systems (Figures 9 and 10). The flow systems in the model include an entrained flow beneath the flat subducting portion of the YT (Area A), a slab rollback driven toroidal flow system that includes a trench-parallel flow in the sub-slab region and a branch that goes around the slab edge and enters the mantle wedge, and an eastward continuation of the sub-slab flow after it passes the slab edge. As detailed below, the model can explain the change from trench orthogonal fast orientations in Area A to trench parallel fast orientations in Area C which may respectively suggest trench orthogonal and trench parallel flows, the spatially varying fast orientations with small splitting times in Area B which may indicate interaction of two mantle flow systems with nearly orthogonal directions, and fast orientations in Area D that are parallel to the continuation of the slab contours.

5.1. Entrained Flow Beneath the Flat-Subducting YT

Both modeling and observational studies suggest that when the subducting lithosphere and the underlying asthenosphere are coupled, an entrained flow system reflecting the simple shear between the two layers can be generated, leading to trench-normal fast orientations (Jadamec & Billen, 2012; Russo & Silver, 1994).
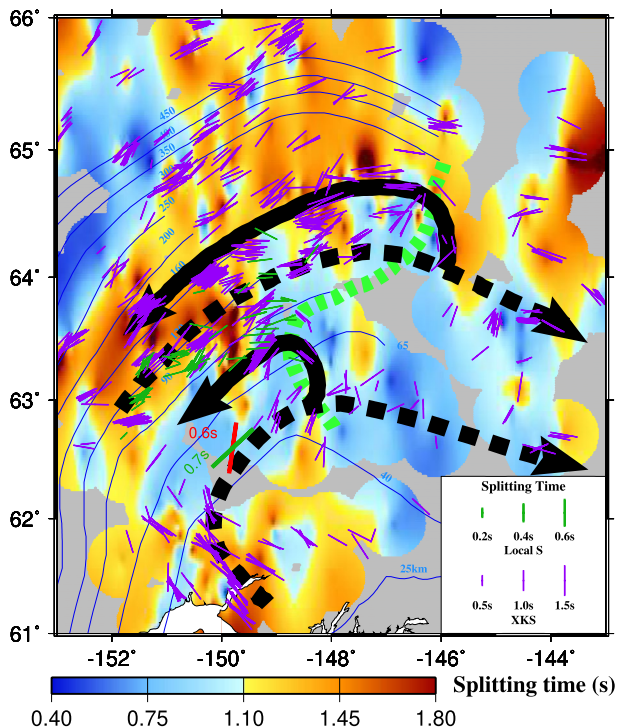
Figure 9. Schematic diagram showing direction of flow lines. The solid lines represent flow entering the mantle wedge from the sub-slab region, and the dashed lines mark the rollback-induced strike-parallel flow beneath the slab and its continued portion. Thin purple and green bars are individual XKS and local S measurements, respectively. The thick red and green bars respectively indicate the lower and upper splitting parameters in the area with two-layered anisotropy. The thick dashed green line is the approximate slab edge, inferred from the spatially varying anisotropy. The background basemap shows spatially smoothed XKS splitting times. The XKS measurements are projected to the depth of nearby slab with a maximum depth of 200 km except for those in the rectangle area shown in Figure 4a, for which a depth of 250 km is used to be consistent with the optimal depth from the spatial coherency analysis (Figure 7). Comparing with the low spatial coherency when they are projected to 200 km depth (Figure 4a), the measurements are spatially more consistent when they are projected at 250 km depth.
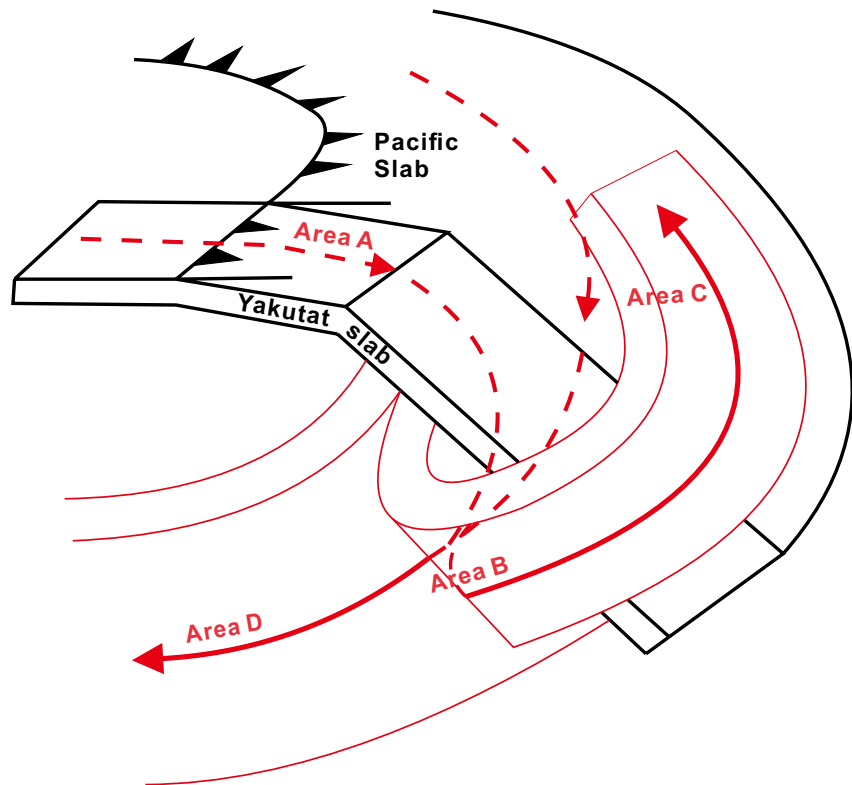
This type of mantle flow has been commonly observed in flat and shallow subduction zones, such as the Peruvian segment of the Peru-Chile subduction zone (Eakin & Long, 2013), the western Hellenic subduction zone (Olive et al., 2014), and the flat-subducting portion of the YT (Christensen & Abers, 2010; Hanna & Long, 2012; McPherson et al., 2020; Perttu et al., 2014; Venereau et al., 2019). The dominantly trench-normal fast orientations observed in Area A can thus be attributed to plastic flow entrained by the flat-subducting YT. Anisotropy in the lower layer obtained using stations in the junction zone of Areas A, B, and C has a nearly N-S fast orientation (Figure 8), which is consistent with the dominant fast orientation in Area A and can also be attributed to entrained flow.

5.2. Sub-Slab Trench Parallel Flow From Slab Rollback

Trench parallel fast orientations observed in the southern part of Area C (approximately to the SE of the 250 km slab depth contour line which represents a transition from a relatively gentle to steep dipping of the slab) can be attributed to sub-slab trench parallel flow induced by slab rollback (e.g., Fouch & Fischer, 1996; Hall et al., 2000; Jadamec & Billen, 2010, 2012; Russo & Silver, 1994) with possible contributions from along-strike variations in slab dip (Kneller & Van Keken, 2008). Due to the high buoyancy of the YT, most studies suggest that slab rollback is insignificant in the study area. However, rollback of the "normal-dipping" section of the Pacific-Yakutat slab to the southwest of the YT has been suggested by some previous studies (e.g., Schellart et al., 2007), which should be capable of producing a sub-slab trench parallel flow that is responsible for the observed trench-parallel anisotropy in the southern part of Area C. Indeed, trench parallel fast orientations have been similarly observed along the entire Alaskan portion of the Aleutian subduction zone (McPherson et al., 2020; Venereau et al., 2019), indicating that variations in slab dip in the study area may not play a significant role in the observed trench parallel fast orientation.

5.3. Contribution of Trench-Parallel Flow in the Mantle Wedge to the Observed Anisotropy

The fast orientations observed in Areas A and C show a drastic variation from trench-perpendicular to trench-parallel. Based on the azimuthal and spatial variations of the SWS results, previous studies indicate that the ~70 km slab depth contour line represents the boundary separating the two fast orientation patterns, reflecting the sub-slab entrained flow and the trench-parallel flow in the wedge, respectively (Christensen & Abers, 2010; Hanna & Long, 2012; McPherson et al., 2020; Perttu et al., 2014; Venereau et al., 2019). However, the average splitting time from the local S measurements is only 0.39 ± 0.13 s, while the XKS results from the same 10 stations show a mean value of 1.25 ± 0.30 s, suggesting that contributions from trench parallel flow in the mantle wedge to the observed anisotropy is about half of that from the sub-slab region. Results from two-layer modeling (Figure 5) for stations in the junction area of Areas A, B, and C also indicate the coexistence of sub-slab and mantle wedge flow in this area. The NE-SW fast orientation for the upper layer may reflect flow in the mantle wedge, and the nearly N-S anisotropy in the lower layer can be attributed to sub-slab flow. It should be mentioned that the splitting time of the upper layer from fitting of the apparent splitting parameters observed in the junction area of Areas A, B, and C is considerably larger (0.7 s) than that from local S wave SWS analysis, possibly due to the fact that the two areas do not exactly overlap, and to the different frequency compositions of the two types of waves.

Figure 10. A three-dimensional schematic model showing the mantle flow fields in the four areas. Solid red arrows represent the flowlines outside of the slab, and dashed arrows indicate those beneath the slab. The two red columns represent the two flow branches. The sawteeth mark the trench of the Alaska subduction zone.

5.4. Continuation of Sub-Slab Mantle Flow Toward the East

The dominantly E-W and WNW-ESE measurements in Area D are in alignment with the local NW-striking strike-slip faults (e.g., Denali Fault in Figure 1a). McPherson et al. (2020) suggest that the anisotropy here is caused by the shear deformation associated with the strike-slip boundary because of the directional similarity between the boundary trend and the fast orientations. The general validity of such an interpretation is essentially based on the hypothesis of vertical coherent deformation (Silver & Chan, 1991) advocating that the lithospheric mantle would deform coherently with the strike-slip processes in the crust and generate progressive simple shear. However, if lithospheric shear zones are the major contributors to the observed anisotropy in Area D, one would expect greater splitting times in areas of known shear zones (such as the Denali Fault). This spatial correspondence is not observed (Figure 9), and thus lithospheric fabrics may not be the major factor in generating the observed anisotropy in this area.

An alternative mechanism for the observed anisotropy in this region is an ESE-ward continuation of the sub-slab flow system, which splits into two branches after passing the slab edge: a toroidal branch entering the mantle wedge (see below), and a continuation branch. In the area immediately to the east of the slab edge (Area B), the moving directions of the two branches are approximately orthogonal to each other, leading to small splitting times (Silver & Savage, 1994).

5.5. Toroidal Mantle Flow Around the Slab Edge

Geodynamic modeling investigations have demonstrated the presence of a toroidal component of mantle flow near a slab edge, where sub-slab trench parallel flow moves around the slab edge and enters the mantle wedge (Jadamec & Billen, 2010, 2012; Kincaid & Griffiths, 2003). However, the predicted flow direction from those geodynamic models in the mantle wedge beneath most part of Area C is trench normal,

which is different from the observed fast orientations of local S waves (which mostly sample the mantle wedge) in this area by ~90°. In addition to the possible reasons for this discrepancy discussed by McPherson et al. (2020), we speculate that the proposed westward increase in the trench retreat rate (from 0.6 cm/yr in south central Alaska to 1.9 cm/yr in the central Aleutians) by Schellart et al. (2007) may cause the transported materials from the sub-slab region to flow further away from the slab edge along the slab. The observed large XKS splitting times and trench parallel fast orientations in Area C (Figure 9) can thus be attributed to the combined effects of two anisotropic layers with similar fast orientations associated with trench-parallel flows in both the mantle wedge and the sub-slab region.

6. Conclusions

SWS measurements from both teleseismic and local events are utilized to constrain mantle flow patterns beneath south central Alaska. The vast majority of the observations, together with results from complex anisotropy analysis and depth estimation of the source of the observed anisotropy, can be explained by a model invoking the splitting of the sub-slab trench-parallel flow into two branches. One of the branches is a continuation of the sub-slab flow system toward the ESE direction, and the other branch flows around the slab edge, enters the mantle wedge, and flows toward the SW along the slab. The two branches are approximately orthogonal to each other in the area immediately to the east of the slab edge, producing spatially varying fast orientations with smaller than normal splitting times.

Data Availability Statement

Data used in the study are all publicly accessible and were requested from the IRIS Data Management Center using the BREQ_FAST approach from http://ds.iris.edu/ds/nodes/dmc/forms/breqfast-request (Last accessed time: XKS 03/2019, Local S: 10/2019). Network codes: AK (https://doi.org/10.7914/SN/AK), AT (https://doi.org/10.7914/SN/AT), DW (https://doi.org/10.7914/SN/DW), IM (International Miscellaneous Stations), IU (https://doi.org/10.7914/SN/IU), TA (https://doi.org/10.7914/SN/TA), XE (https://doi.org/10.7914/SN/XE_1999), XR (https://doi.org/10.7914/SN/XR_2004), XV (https://doi.org/10.7914/SN/XV_2014), YE (https://doi.org/10.7914/SN/YE_2011), and YV (https://doi.org/10.7914/SN/YV_2006). IRIS Data Services are funded through the Seismological Facilities for the Advancement of Geoscience (SAGE) Award of the National Science Foundation under Cooperative Support Agreement EAR-1851048.

References

Alsina, D., & Snieder, R. (1995). Small-scale sublithospheric continental mantle deformation: Constraints from SKS splitting observations. *Geophysical Journal International*, *123*, 431–448. https://doi.org/10.1111/j.1365-246x.1995.tb06864.x

Ando, M. (1984). ScS polarization anisotropy around the Pacific Ocean. *Journal of Physics of the Earth*, *32*, 179–195. https://doi.org/10.4294/jpe1952.32.179

Cherie, S. G., Gao, S. S., Liu, K. H., Elsheikh, A. A., Kong, F., Reed, C. A., & Yang, B. B. (2016). Shear wave splitting analyses in Tian Shan: Geodynamic implications of complex seismic anisotropy. *Geochemistry, Geophysics, Geosystems*, *17*, 1975–1989. https://doi.org/10.1002/2016GC006269

Chevrot, S. (2006). Finite-frequency vectorial tomography: A new method for high-resolution imaging of upper mantle anisotropy. *Geophysical Journal International*, *165*, 641–657. https://doi.org/10.1111/j.1365-246X.2006.02982.x

Christensen, D. H., & Abers, G. A. (2010). Seismic anisotropy under central Alaska from SKS splitting observations. *Journal of Geophysical Research*, *115*, B04315. https://doi.org/10.1029/2009JB006712

Civello, S., & Margheriti, L. (2004). Toroidal mantle flow around the Calabrian slab (Italy) from SKS splitting. *Geophysical Research Letters*, *31*(10), L10601. https://doi.org/10.1029/2004GL019607

Currie, C. A., Cassidy, J. F., Hyndman, R. D., & Bostock, M. G. (2004). Shear wave anisotropy beneath the Cascadia subduction zone and western North America craton. *Geophysical Journal International*, *157*, 341–353. https://doi.org/10.1111/j.1365-246X.2004.02175.x

Dahm, H. H., Gao, S. S., Kong, F., & Liu, K. H. (2017). Topography of the mantle transition zone discontinuities beneath Alaska and its geodynamic implications: Constraints from receiver function stacking. *Journal of Geophysical Research: Solid Earth*, *122*(12), 10352–10363. https://doi.org/10.1002/2017JB014604

Eakin, C. M., & Long, M. D. (2013). Complex anisotropy beneath the Peruvian flat slab from frequency-dependent, multiple-phase shear wave splitting analysis. *Journal of Geophysical Research: Solid Earth*, *118*, 4794–4813. https://doi.org/10.1002/jgrb.50349

Eberhart-Phillips, D., Christensen, D. H., Brocher, T. M., Hansen, R., Ruppert, N. A., Haeussler, P. J., & Abers, G. A. (2006). Imaging the transition from Aleutian subduction to Yakutat collision in central Alaska, with local earthquakes and active source data. *Journal of Geophysical Research*, *111*, B11303. https://doi.org/10.1029/2005JB004240

Feng, L., Liu, C., & Ritzwoller, M. H. (2020). Azimuthal anisotropy of the crust and uppermost mantle beneath Alaska. *Journal of Geophysical Research: Solid Earth*, *125*, e2020JB020076. https://doi.org/10.1029/2020JB020076

Ferris, A., Abers, G. A., Christensen, D. H., & Veenstra, E. (2003). High resolution image of the subducted Pacific (?) plate beneath central Alaska, 50-150 km depth. *Earth and Planetary Science Letters*, *214*(3–4), 575–588. https://doi.org/10.1016/S0012-821X(03)00403-5

Fouch, M. J., & Fischer, K. M. (1996). Mantle anisotropy beneath northwest Pacific subduction zones. *Journal of Geophysical Research: Solid Earth*, *101*(B7), 5987–1600. https://doi.org/10.1029/96jb00881

Gao, S. S., & Liu, K. H. (2012). AnisDep: A FORTRAN program for the estimation of the depth of anisotropy using spatial coherency of shear-wave splitting parameters. *Computers & Geosciences*, *49*, 330–333. https://doi.org/10.1016/j.cageo.2012.01.020

Gou, T., Zhao, D., Huang, Z., & Wang, L. (2019). Aseismic deep slab and mantle flow beneath Alaska: Insight from anisotropic tomography. *Journal of Geophysical Research: Solid Earth*, *124*, 1700–1724. https://doi.org/10.1029/2018JB016639

Hall, C. E., Fischer, K. M., Parmentier, E. M., & Blackman, D. K. (2000). The influence of plate motions on three-dimensional back arc mantle flow and shear wave splitting. *Journal of Geophysical Research*, *105*, 28009–28033. https://doi.org/10.1029/2000jb900297

Hanna, J., & Long, M. D. (2012). SKS splitting beneath Alaska: Regional variability and implications for subduction processes at a slab edge. *Tectonophysics*, *530–531*, 272–285. https://doi.org/10.1016/j.tecto.2012.01.003

Hess, H. H. (1964). Seismic anisotropy of the uppermost mantle under oceans. *Nature*, *203*, 629–631. https://doi.org/10.1038/203629a0

Jadamec, M. A., & Billen, M. I. (2010). Reconciling surface plate motions with rapid three-dimensional mantle flow around a slab edge. *Nature*, *465*, 338–341. https://doi.org/10.1038/nature09053

Jadamec, M. A., & Billen, M. I. (2012). The role of rheology and slab shape on rapid mantle flow: Three-dimensional numerical models of the Alaska slab edge. *Journal of Geophysical Research: Solid Earth*, *117*, B02304. https://doi.org/10.1029/2011JB008563

Jia, Y., Liu, K. H., Kong, F., Liu, L., & Gao, S. S. (2021). A systematic investigation of piercing point dependent seismic azimuthal anisotropy. *Geophysical Journal International*, *227*, 1496–1511. https://doi.org/10.1093/gji/ggab285

Jiang, C., Schmandt, B., Ward, K. M., Lin, F. C., & Worthington, L. L. (2018). Upper mantle seismic structure of Alaska from Rayleigh and S wave tomography. *Geophysical Research Letters*, *45*(19), 10350–10359. https://doi.org/10.1029/2018GL079406

Jiang, E., Liu, K. H., Gao, Y., Fu, X., & Gao, S. S. (2021). Spatial variations of upper crustal anisotropy along the San Jacinto Fault Zone in Southern California: Constraints from shear wave splitting analysis. *Journal of Geophysical Research: Solid Earth*, *126*, e2020JB020876. https://doi.org/10.1029/2020JB020876

Karlowska, E., Bastow, I. D., Rondenay, S., Martin-Short, R., & Allen, R. M. (2021). The development of seismic anisotropy below south-central Alaska: Evidence from local earthquake shear wave splitting. *Geophysical Journal International*, *225*(1), 548–554. https://doi.org/10.1093/gji/ggaa603

Kennett, B. L. N., & Engdahl, E. R. (1991). Travel times for global earthquake location and phase association. *Geophysical Journal International*, *105*, 429–465. https://doi.org/10.1111/j.1365-246X.1991.tb06724.x

Kincaid, C., & Griffiths, R. W. (2003). Laboratory models of the thermal evolution of the mantle during rollback subduction. *Nature*, *425*(6953), 58–62. https://doi.org/10.1038/nature01923

Kneller, E. A., & van Keken, P. E. (2008). Effect of three-dimensional slab geometry on deformation in the mantle wedge: Implications for shear wave anisotropy. *Geochemistry, Geophysics, Geosystems*, *9*, Q01003. https://doi.org/10.1029/2007GC001677

Kong, F., Gao, S. S., Liu, K. H., Ding, W. W., & Li, J. (2020). Slab dehydration and mantle upwelling in the vicinity of the Sumatra subduction zone: Evidence from receiver function imaging of mantle transition zone discontinuities. *Journal of Geophysical Research: Solid Earth*, *125*, e2020JB019381. https://doi.org/10.1029/2020JB019381

Kong, F., Wu, J., Liu, L., Liu, K. H., Song, J., Li, J., & Gao, S. S. (2018). Azimuthal anisotropy and mantle flow underneath the southeastern Tibetan Plateau and northern Indochina Peninsula revealed by shear wave splitting analyses. *Tectonophysics*, *747–748*, 68–78. https://doi.org/10.1016/j.tecto.2018.09.013

Liu, K. H., & Gao, S. S. (2011). Estimation of the depth of anisotropy using spatial coherency of shear-wave splitting parameters. *Bulletin of the Seismological Society of America*, *101*, 2153–2161. https://doi.org/10.1785/0120100258

Liu, K. H., & Gao, S. S. (2013). Making reliable shear-wave splitting measurements. *Bulletin of the Seismological Society of America*, *103*(5), 2680–2693. https://doi.org/10.1785/0120120355

Liu, K. H., Gao, S. S., Gao, Y., & Wu, J. (2008). Shear wave splitting and mantle flow associated with the deflected Pacific slab beneath northeast Asia. *Journal of Geophysical Research*, *113*, B01305. https://doi.org/10.1029/2007JB005178

Long, M. D., & Becker, T. W. (2010). Mantle dynamics and seismic anisotropy. *Earth and Planetary Science Letters*, *297*(3–4), 341–354. https://doi.org/10.1016/j.epsl.2010.06.036

Long, M. D., & Silver, P. G. (2008). The subduction zone flow field from seismic anisotropy: A global view. *Science*, *319*(5861), 315–318. https://doi.org/10.1126/science.1150809

Long, M. D., & Silver, P. G. (2009). Shear wave splitting and mantle anisotropy: Measurements, interpretations, and new directions. *Surveys in Geophysics*, *30*(4–5), 407–461. https://doi.org/10.1007/s10712-009-9075-1

Martin-Short, R., Allen, R., Bastow, I. D., Porritt, R. W., & Miller, M. S. (2018). Seismic imaging of the Alaska subduction zone: Implications for slab geometry and volcanism. *Geochemistry, Geophysics, Geosystems*, *19*(11), 4541–4560. https://doi.org/10.1029/2018GC007962

McPherson, A. M., Christensen, D. H., Abers, G. A., & Tape, C. (2020). Shear wave splitting and mantle flow beneath Alaska. *Journal of Geophysical Research: Solid Earth*, *123*, e2019JB018329. https://doi.org/10.1029/2019jb018329

Olive, J. A., Pearce, F., Rondenay, S., & Behn, M. D. (2014). Pronounced zonation of seismic anisotropy in the Western Hellenic subduction zone and its geodynamic significance. *Earth and Planetary Science Letters*, *391*, 100–109. https://doi.org/10.1016/j.epsl.2014.01.029

Paczkowski, K., Montési, L. G. J., Long, M. D., & Thissen, C. J. (2014). Three-dimensional flow in the subslab mantle. *Geochemistry, Geophysics, Geosystems*, *15*, 3989–4008. https://doi.org/10.1002/2014GC005441

Palano, M., Piromallo, C., & Chiarabba, C. (2017). Surface imprint of toroidal flow at retreating slab edges: The first geodetic evidence in the Calabrian subduction system. *Geophysical Research Letters*, *44*(2), 845–853. https://doi.org/10.1002/2016GL071452

Perttu, A., Christensen, D., Abers, G., & Song, X. (2014). Insights into mantle structure and flow beneath Alaska based on a decade of observations of shear wave splitting. *Journal of Geophysical Research: Solid Earth*, *119*, 8366–8377. https://doi.org/10.1002/2014JB011359

Ribe, N. M., & Yu, Y. (1991). A theory for plastic deformation and textural evolution of olivine polycrystals. *Journal of Geophysical Research: Solid Earth*, *96*, 8325–8335. https://doi.org/10.1029/90jb02721

Russo, R. M., & Silver, P. G. (1994). Trench-parallel flow beneath the Nazca plate from seismic anisotropy. *Science*, *263*(5150), 1105–1111. https://doi.org/10.1126/science.263.5150.1105

Schellart, W. P. (2004). Kinematics of subduction and subduction-induced flow in the upper mantle. *Journal of Geophysical Research*, *109*(7), B07401. https://doi.org/10.1029/2004JB002970

Schellart, W. P., Freeman, J., Stegman, D. R., Moresi, L., & May, D. (2007). Evolution and diversity of subduction zones controlled by slab width. *Nature*, *446*(7133), 308–311. https://doi.org/10.1038/nature05615

Silver, P. G. (1996). Seismic anisotropy beneath the continents: Probing the depths of geology. *Annual Review of Earth and Planetary Sciences*, *24*, 385–432. https://doi.org/10.1146/annurev.earth.24.1.385

Silver, P. G., & Chan, W. W. (1991). Shear wave splitting and subcontinental mantle deformation. *Journal of Geophysical Research*, *96*(B10), 16429–16454. https://doi.org/10.1029/91jb00899

Silver, P. G., & Savage, M. K. (1994). The interpretation of shear-wave splitting parameters in the presence of two anisotropic layers. *Geophysical Journal International*, *119*, 949–963. https://doi.org/10.1111/j.1365-246x.1994.tb04027.x

Stegman, D. R., Freeman, J., Schellart, W. P., Moresi, L., & May, D. (2006). Influence of trench width on subduction hinge retreat rates in 3-D models of slab rollback. *Geochemistry, Geophysics, Geosystems*, *7*, Q03012. https://doi.org/10.1029/2005GC001056

Tian, Y., & Zhao, D. (2012). Seismic anisotropy and heterogeneity in the Alaska subduction zone. *Geophysical Journal International*, *190*(1), 629–649. https://doi.org/10.1111/j.1365-246X.2012.05512.x

Venereau, C. M. A., Martin-Short, R., Bastow, I. D., Allen, R. M., & Kounoudis, R. (2019). The role of variable slab dip in driving mantle flow at the eastern edge of the Alaskan subduction margin: Insights from shear-wave splitting. *Geochemistry, Geophysics, Geosystems*, *20*, 2433–2448. https://doi.org/10.1029/2018GC008170

Vinnik, L. P., Makeyeva, L. I., Milev, A., & Usenko, A. Y. (1992). Global patterns of azimuthal anisotropy and deformations in the continental mantle. *Geophysical Journal International*, *111*(3), 433–447. https://doi.org/10.1111/j.1365-246X.1992.tb02102.x

Worthington, L. L., Van Avendonk, H. J. A., Gulick, S. P. S., Christeson, G. L., & Pavlis, T. L. (2012). Crustal structure of the Yakutat terrane and the evolution of subduction and collision in southern Alaska. *Journal of Geophysical Research: Solid Earth*, *117*(1), B01102. https://doi.org/10.1029/2011JB008493

Yang, B. B., Gao, S. S., Liu, K. H., Elsheikh, A. A., Lemnifi, A. A., Refayee, H. A., & Yu, Y. (2014). Seismic anisotropy and mantle flow beneath the northern Great Plains of North America. *Journal of Geophysical Research: Solid Earth*, *119*, 1971–1985. https://doi.org/10.1002/2013JB010561

Zhang, S., & Karato, S. (1995). Lattice preferred orientation of olivine aggregates deformed in simple shear. *Nature*, *375*, 774–777. https://doi.org/10.1038/375774a0